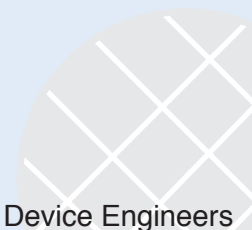


Simulation Standard



Engineered Excellence

A Journal for Process and Device Engineers

Design Consideration & Performance Analysis of MCT Based Dual Band (MWIR/LWIR) Photodetector

Abstract

In this paper, a physics based two dimensional (2-D) generic model of dual band mid wavelength and long wavelength infrared (MW-LW) photodetector based on HgCdTe has been reported. The paper discusses variants of the back-to-back diode structure, which allows the detected waveband to be selected simply without changing the polarity of the bias. The structure has been designed by exploiting 2D SILVACO software. A closed form model has been developed for electrical and optical characterization of the device. The model includes all the relevant material physics and solution of non-linear decoupled semiconductor transport and Poisson's equations. The results obtained on the basis of numerical simulation have been validated with the reported analytical and experimental results by the others. Good agreement is found between both.

Key words: Dualband, MWIR, LWIR, Hetero-interface, HgCdTe-MCT.

1. Introduction

Mercury-Cadmium-Telluride (HgCdTe) is the dominant material for development of high sensitivity infrared photodetectors for military applications, medical imaging, fire control, environment monitoring and surveillance, and amongst other applications. The adjustable energy gap of HgCdTe with sensitivity spanning from short wavelength (SWIR) to very long wavelength (VLWIR) infrared bands enables it for tremendous potential applications to be realized using advance material growth methods and different detectors design. Significant progress has been made towards the growth of unispectral HgCdTe photodetectors in MWIR and LWIR applications during last five decades. The requirement of the new generation of IR detectors is currently under development, e.g. dual band photodetectors, i.e. two color detection simultaneously. Although unispectral photodetectors can serve separately, but two color detectors offer better performance for same applications.

Initially, the problem in development of dual band photodetector with bias selectable device i.e. independent selection of the optimum bias voltage for both photodiode and substantial medium wavelength (MW) crosstalk in the long wavelength (LW) detector.

These problems associated with dual band detector can be solved by optimizing design guidelines and the device parameters. The dual band detector cannot be designed and optimized by using 1D model because several additional physical phenomena needed to define the mechanisms inside the device. It is important to point out that a very few attempts have been made to perform two dimensional (2-D) simulations of these advanced devices. The biggest challenge is to minimize crosstalk effects within the nearest two photodetectors. It is important to develop a physics based model that can quantitatively estimate the cross talk and provide useful design guidelines for minimization of cross talk [1] – [2]

2. Design and 2-D Simulation of MW/LW Dual Band Detector

Figure 1a shows the two dimensional cross-sectional view of a dual band photodetector consisting of back-to-back photodiodes. The five layer device composed of two HgCdTe p-n junctions with different energy bandgap. A thin layer has been sandwiched between two diodes. The structure has been designed by using ATLAS framework

Continued on page 2 ...

INSIDE

<i>The Doping Effect Simulation on the OLED Devices Using ATLAS.....</i>	<i>7</i>
<i>Using VICTORY Process to Simulate Thermal Oxidation of Silicon at High Pressures of Ambient Gases</i>	<i>10</i>
<i>Hints, Tips and Solutions</i>	<i>12</i>

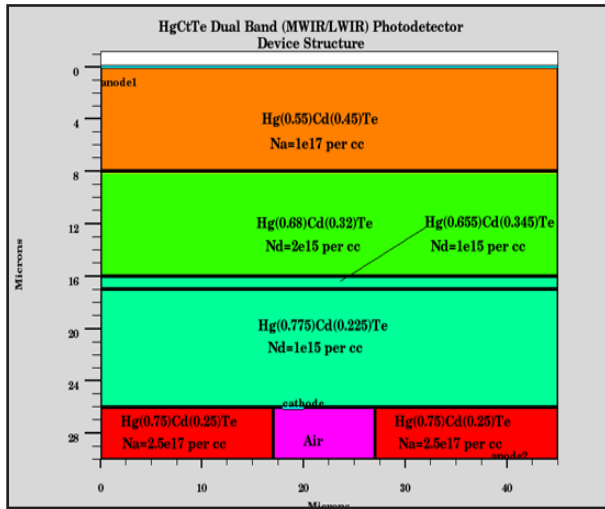


Figure 1a. Dual Band (MWIR/LWIR) Photodetector Device Structure.

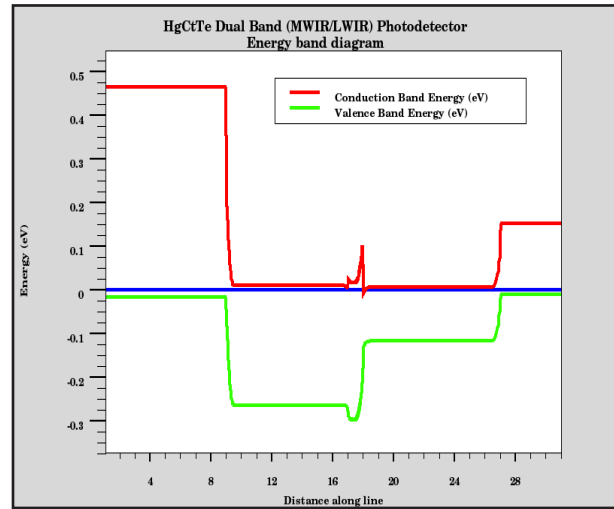


Figure 1b. Simulated Energy band diagram.

interfaced with BLAZE of the SILVACO (Figure 1b) for electrical characterization. The Luminous module has been used to design a multi-spectral source and for optical characterization. [3].

The bottom P-N junction (upper case indicate wide band-gap material), has grown such that pixel mesa is square with dimension $45 \times 45 \mu\text{m}$ and mole fraction (x) of $\text{Hg}_x\text{Cd}_{1-x}\text{Te}$ material is taken for cutoff wavelength $4.3 \mu\text{m}$. The doping concentrations of P- and N-layers are $1 \times 10^{23} \text{m}^{-3}$ and $2 \times 10^{21} \text{m}^{-3}$ respectively. An n-type buffer layer is deposited over P-N junction. The doping density of the buffer layer is taken to be $1 \times 10^{21} \text{m}^{-3}$ with mole fraction $x=0.345$ to minimize the crosstalk between MW band to LW detector. The narrow bandgap n-type layer is deposited on buffer layer with pixel mesa dimension $45 \times 45 \mu\text{m}$ followed by deposition of p-type layer over it with mesa pixel dimension $45 \times 45 \mu\text{m}$. The cut off wave length of LWIR detector has been tuned $10.34 \mu\text{m}$ by choosing appropriate mole fraction (x) value.

The p-type layer is etched within structure to make common cathode contact to both detectors. The other two anode contacts have been taken on the bottom of P-type and top of p-type materials. The main advantage of this design was to use narrow gap n-type HgCdTe buffer layer to limit the crosstalk between two photodiodes. The selected mole fraction and doping concentration of all the layers ensure the best compromise between requirements of effective absorption of IR radiation and low thermal generation of charge carriers. The light is incident through MWIR detector.

In the simulation of energy band of the heterostructure using ATLAS, it is assumed that the ground state degeneracy of conduction band g_c and valance band g_v are 2 and 4 respectively. The analysis of energy band diagram of hetero-junction shows that there is energy

offset in the conduction ΔE_C and valance band ΔE_V due to electron affinity differences and doping concentration gradient and justifies the application of Anderson's rule. The formation of potential barrier within heterojunction at the buffer layer can be understood in terms of forces that arise due to gradient in electrostatic potential ∇V and electron affinity $\nabla \chi$. The electrons will be the dominant current carriers because the barrier is smaller for electrons as compared to holes. The drop in energy band at n-n heterojunction accompanies the potential variation at interface of the junction. The height of the potential barrier at n-n heterojunction depends on the doping profile of the material. [4]- [5]

In device characterization, (both electrical and optical) the basic non linear decoupled equations have been solved. Numerical simulation has been done for degenerate semiconductor and non-parabolic shape of conduction band. The results presented in this work are obtained with ATLAS (Blaze 2D) software of SILVACO. The Newton-Richardson iteration technique has been used to solve five nonlinear decoupled equations. The Newton-Richardson based method improves the efficiency of the iteration [3].

The doping of the regions has been taken analytically uniform for all regions in the above simulation. In calculation of mobility the concentration dependent ANALYTIC model has been considered. For the simulation of dark current associated with LWIR p-n heterojunction photodetector, AUGER, SRH and OPTICAL (band-to-band) models have been taken into account for recombination mechanisms. Band-to-band standard tunneling and trap assisted tunneling models have been considered for tunneling mechanism. We have taken into account the Fermi-Dirac statistics for non-parabolic shape of conduction band in all the calculations of carrier and doping densities.

3. Numerical Simulation

3.1 Dark Current

Basic semiconductor transport equations (continuity equations for holes and electrons) and Poisson's equations have been used for the numerical analysis. The following equation can be given as [5]

$$\frac{\delta n}{\delta t} - \frac{1}{q} \nabla J_n + (G_n - R_n) \quad \text{Continuity equation for electrons} \quad (1)$$

$$\frac{\delta p}{\delta t} - \frac{1}{q} \nabla J_p + (G_p - R_p) \quad \text{Continuity equation for holes} \quad (2)$$

$$\text{div}(\epsilon_s \nabla V) = -\rho \quad \text{Poisson's equation} \quad (3)$$

where n and p are the electron and hole concentration, J_n and J_p are the electron and hole current densities, G_n and G_p are the generation rates for electron and holes, R_n and R_p are the recombination rates for electrons and holes, and q is the magnitude of the charge on the electron. V is the electrostatic potential, ϵ_s is the local permittivity and ρ is the local space charge density.

The solution of equation (1) to (3) involves drift and diffusion components. The current flowing through each heterostructure photovoltaic dualband detector under consideration has three major components:

- i) The diffusion current arising from the minority carriers injected from the each neutral p and n regions;
- ii) The drift current arising from generation recombination in the depletion region at the each p - n junction and n - n junctions;
- iii) The tunneling current across the p - n heterointerface.

The magnitude of total dark current of the photodetector is [5]

$$I_{DARK} = I_{DIFF} + I_{GR} + I_{TUN} \quad (4)$$

3.2 Spectral Response

The spectral response of the dual band photodetector has been predicted in terms of quantum efficiency. The quantum efficiency can be obtained by using multilayer approach in which the electric field should be matched at the interfaces and structure is supposed to have number of layers with constant complex refractive index. The inter-diffusion layers at each metallurgical interface with continuous variation in the composition, results in cross talk at these interfaces [4] – [5].

Here, quantum efficiency is defined as the ratio of the number of carriers detected at a given photodetector electrode divided by the number of incident photons on the detector. The absorption coefficient ' α ' is calculated in terms of complex refractive index of each region separately. Different refractive index files have been used for different composition of the MCT materials. The absorption coefficient plays an essential part in deciding the spectral response of the both MW/LW detectors. The available photocurrent within the device can be calculated with the help of absorption coefficient [3].

4. Results and Discussion

The simulation of dualband photodetector uses ATLAS tool in conjunction with Blaze module for developing the structure based on compound semiconductors, for electrical characterization and the Luminous module for optical characterization. In the numerical simulation of various characteristics of the heterojunction dualband photodetector, all the calculations have been done by using appropriate material parameters, dependent on the mole fraction (x) of different $\text{Hg}_{1-x}\text{Cd}_x\text{Te}$ layers are listed in Appendix 1.1.

Numerical computations have been carried out for electrical and optical characterization of dualband heterojunctions $p\text{-Hg}_{0.75}\text{Cd}_{0.25}\text{Te}/n\text{-Hg}_{0.775}\text{Cd}_{0.225}\text{Te}/n\text{-Hg}_{0.665}\text{Cd}_{0.345}\text{Te}/N\text{-Hg}_{0.68}\text{Cd}_{0.32}\text{Te}/P\text{-Hg}_{0.55}\text{Cd}_{0.45}\text{Te}/\text{CdZnTe}$ photodetector at 77K for operation at MWIR region (2-5 μm) and LWIR region (8-14 μm) simultaneously. The photons with energy higher than the energy gap create electron-hole pairs in each neutral p and n regions as well as in depletion regions formed at the all metallurgical junction.

Chu's model [6] has been used to calculate optical absorption coefficients (α_n & α_p) in determining the imaginary part of the optical index of refraction (k) are given in Appendix 1.1.

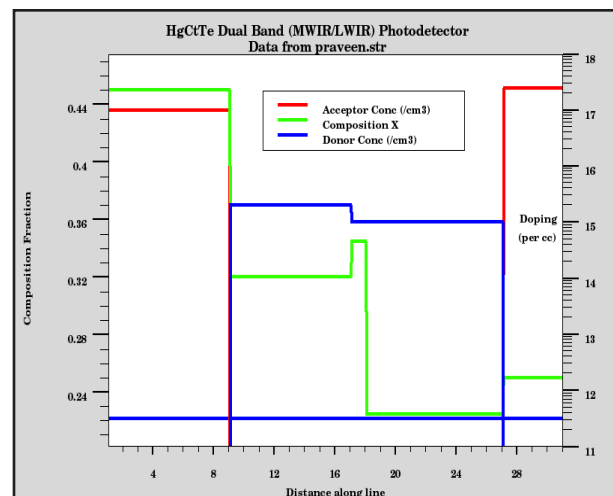


Figure 2. Simulated Doping & Composition Profile.

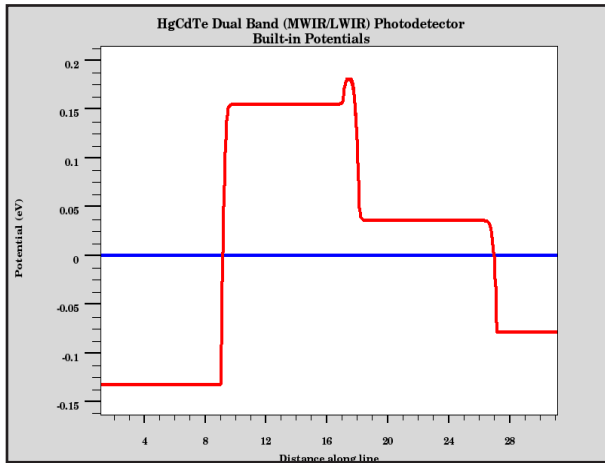


Figure 3a. Simulated Electrical Potential profile in absence of external biasing.

The structure under consideration consists of five layers p-n-n-N-P heterostructure based on HgCdTe for MW/LW detection simultaneously is shown in Fig. 1a. The simulated energy band diagram is shown in Fig. 1b. The Anderson type discontinuities have been observed at each hetero-interface. A thin n-type compositional barrier layer is placed between MW and LW absorber layers. This barrier layer forms an n-N heterojunction at the interface. The barrier layer thickness can be optimized such that it would prevent the MW photocarriers from diffusing into the LW absorber layer and prevents LW photocarriers from diffusing into the MW absorber layer. The crosstalk effect between MW and LW bands has been calculated in present model. Under reverse bias photodetector behaves as non-equilibrium device. The analysis has been carried out for non-equilibrium mode by considering quasi-Fermi level into account.

The variation of composition x and doping profile has been depicted in Figure 2. The profile of the electrical potential V across the dualband photodetector at each metallurgical hetero-junction and all neutral regions, in absence of infrared radiation flux and external bias, is shown in Fig-

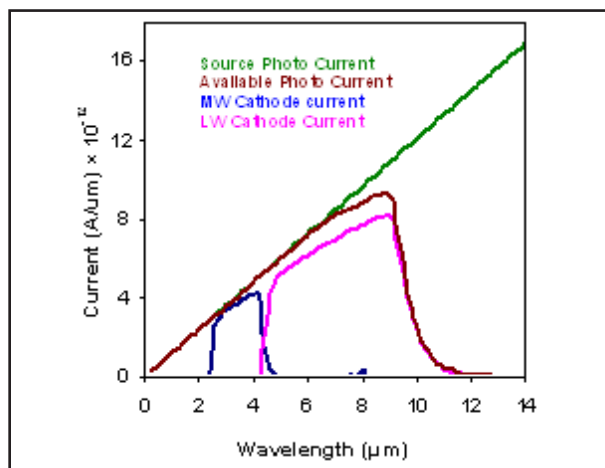


Figure 4. Variation of different currents with operating wavelength.

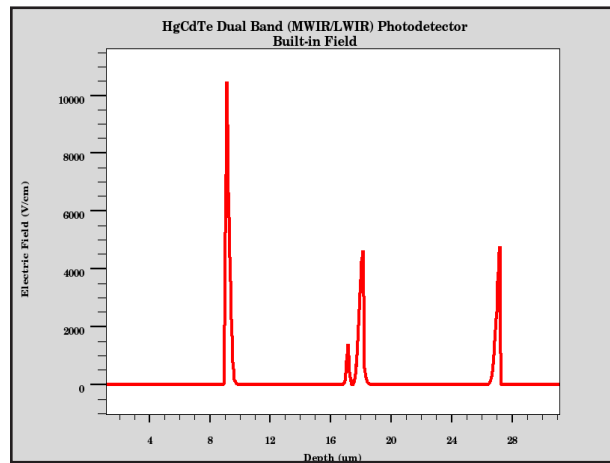


Figure 3b. Simulated Electrical Field profile in absence of external biasing.

ure 3a. The results have been verified against the theoretical results reported by Rogalski *et. al.*, in reference [1].

The electric field associated with the dualband photodetector, gives a perfect triangular shape at each metallurgical junction. The maximum value of electric field (Figure 3b) of the order of 10^6 V/m is obtained for MW hetero-junction photodetector. A separate peak is observed at n-N isotype hetero-interface due to buffer layer which acts as a barrier in path of carriers diffusing from MW to LW region and vice-versa and minimizes the crosstalk effect. The value of electric field at LW hetero-interface is comparatively low.

The distribution of source photocurrent, available photocurrent (due to absorption of photons) and cathode currents produced within the simulated device has been compared in Figure 4. A multispectral source has also been designed on Luminous platform, for two color detection operation. The power density (P_{opt}) of the source has been kept constant. In the 0.2-10 μm wavelength region source photocurrent and available photocurrent almost overlap on each other. In 0.2-2 μm wavelength region the magnitude of cathode current is almost negligi-

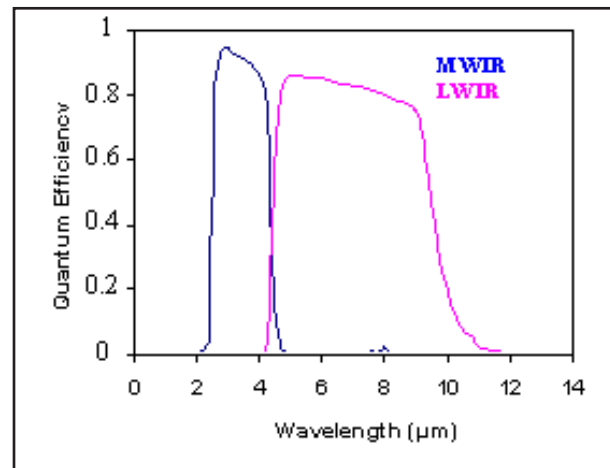


Figure 5. Variation of theoretically computed quantum efficiency with wavelength.

Parameters	MWIR		LWIR	
	Theoretical	Experimental	Theoretical	Experimental
Cutoff wavelength (μm)	4.3	4.29	10.33	10.33
Quantum efficiency (η)	94%	79%	86%	67%

Table 1. Comparison between experimental data with the theoretically calculated data.

ble and shows no influence over available photocurrent. The cathode current increases for the operative wavelength region under zero biasing condition. The available photocurrent suddenly drops after the maximum cutoff wavelength (10.34 μm) of the LW detector because the designing has been done by optimizing the device parameters for operation at MW and LW bands only.

The spectral dependence of quantum efficiency, as a function of operating wavelength, for MW and LW photodetector at 77K is shown in Figure 5. It is seen that MW heterojunction $\text{P-Hg}_{0.55}\text{Cd}_{0.45}\text{Te/N-Hg}_{0.68}\text{Cd}_{0.32}\text{Te}$ photodetector under consideration exhibits almost constant efficiency in entire MWIR region (2.2- 4.3 μm), which is desirable. The maximum internal quantum efficiency exhibited by MW detector is 94%. The quantum efficiency falls very fast beyond the long wavelength cut-off. The LW detector shows almost constant efficiency within wavelength range (4-10.5 μm). The maximum internal quantum efficiency exhibited by LW detector at near cut off wavelength is 86%. The internal quantum efficiency of the both devices has been obtained by rigorous computations. The MW detector shows better spectral response as compared to LW detector. The crosstalk (defined as the ratio of LW available photocurrent to MW available photocurrent in absence of LW radiation) occurs in the LW photodetector, which is less than 4%, and is due to absence of effective barrier for minority carriers (in this case hole of the MW detector. The crosstalk effect has been relatively reduced by optimizing the separation between MW and LW spectral response. A comparison has been made between experimental reported data with the simulation results given in Table 1.

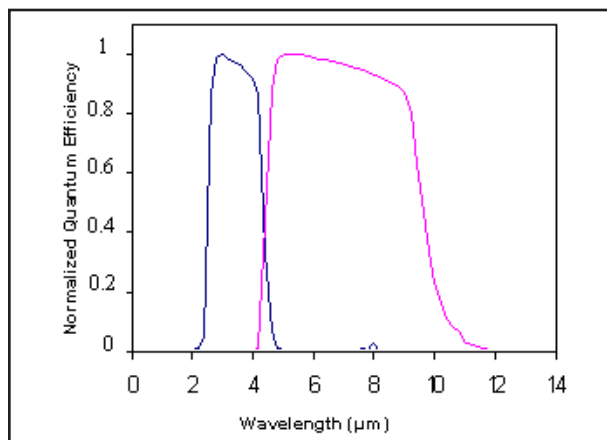


Figure 6. Variation of normalized quantum efficiency with operating wavelength.

The simulated results of relative spectral response of designed MW/LW HgCdTe detector have been compared and contrasted with the experimental reported data [2] is shown in Figure 6. The calculated quantum efficiency depends on the dimension of the shorting contact on which common contact is deposited. Small changes in size affect the quantum efficiency significantly. The average cutoff wavelengths of MW and LW detectors at 77K are 4.3 μm and 10.33 μm respectively. The crosstalk effect has been reduced in present modeling of MW/LW photodetector because relative quantum efficiency is very low for wavelengths beyond 4.4 μm , which can be clearly seen from the figure.

The theoretically obtained cross talk (< 4%) effect is consistent with the experimental reported value. The MW to LW cross talk has been seen in 4.0-4.8 μm wavelength region. The relative quantum efficiency of MW detector in shorter wavelength region is very low because of high recombination rate of the generated photocarriers at the interface between wide-gap P-type layer. The LW relative spectral response increases sharply beyond 4.0 μm . The value of theoretically predicted relative quantum efficiency is close to experimentally measured values for the both MW and LW detectors.

6. Conclusion

In present paper, the performance of simultaneous two-color MWIR-LWIR HgCdTe based photovoltaic detector has been simulated numerically using SILVACO software. The photodetector has been designed and optimized for two colors simultaneously detection applications. A numerical simulation technique has been used to solve the system of decoupled nonlinear equations and Poisson equation. The results of the 2-D simulation of dualband detector show that it is possible to predict the performance of complex detector with fairly good accuracy. The LW detector exhibits lower QE because of much of higher noise current density. The analysis of QE shows that the considerable cross talk between MW band and LW band exists. The simulation of the two color heterojunction photodetector provides useful electrical and optical behavior of the device. The model can be used for optimization of HgCdTe based dualband photodetectors for multi spectral detection application. The magnitude of simulated dark current has a very low value near zero bias. The simulated results can be used as design guidelines by the engineers for developing device prototype which in turn

will reduce the number of experimental trails required for the development of improved heterojunction photodetectors based on HgCdTe. Finally, the theoretically predicted spectral characteristics are found to be in good agreement with the reported experimental data.

Appendix 1.1

A program has been developed for simulation of two dimensional abrupt p-n heterojunction device based on HgCdTe. The formula used in calculations of band gap energy, effective mass, mobilities of charge carriers, electron affinity, and absorption coefficient (using nonparabolic model) as a function of mole fraction (x) of Cd in HgCdTe alloy and temperature are given below.

$$E_g = -0.302 + 1.93x - 0.81x^2 + 0.832x^3 + 5.35 \times 10^{-4}(1-2x)T \quad (5)$$

$$x = 4.23 - 0.813 (E_g - 0.083) \quad (6)$$

$$\mu_n = 9 \times 10^8 (0.2/x)^{7.5} T^{-2} \left(\frac{0.2}{x}\right)^{0.6} \quad (7)$$

$$\frac{m_n^*}{m_0} = \left[-0.6 + 6.333 \left(\frac{2}{E_g} + \frac{1}{E_g + 1} \right) \right]^{-1} \quad (8)$$

$$\frac{m_p^*}{m_0} = 0.55 \quad (9)$$

$$\epsilon_s = 20.5 - 15.5x + 5.7x^2 \quad (10)$$

The effective Richardson constant is defined as

$$R^* = \frac{4\pi q k^2 m^*}{h^3} \quad (11)$$

The Kramers and Kronig interrelations are usually used to estimate the dependence of refractive index on temperature. For Hg_{1-x}Cd_xTe with x from 0.276 to 0.540 and temperatures from 4.2 to 300 K, the following empirical formula can be used

$$n^2(\lambda, T) = A + \left(\frac{B}{1 - (\frac{\lambda}{\lambda_c})^2} \right) + D\lambda^2 \quad (12)$$

where

$$A = 13.173 - 9.852x + 2.909x^2 + (300 - T)10^{-3};$$

$$B = 0.83 - 0.246x - 0.0961x^2 + (300 - T)8e-4;$$

$$C = 6.706 - 14.437x + 8.531x^2 + (300 - T)7e-4;$$

$$D = 1.953e-4 - 0.00128x + 1.853e-4x^2;$$

Imaginary part of refractive index can be obtained using following relation

$$K = \frac{\lambda}{4\pi} \alpha \quad (13)$$

Absorption Coefficient

Investigations of the measured absorption coefficient α of Hg_{1-x}Cd_xTe near the band edge show that the frequency dependence of α follows a modified Urbach rule of the form [6]

$$\alpha = \alpha_0 \exp \left(\frac{\delta(E - E_0)}{kT} \right) \quad (14)$$

where

$$\ln \alpha_0 = -18.5 + 45.68x,$$

$$E_0 = -0.355 + 1.77x,$$

$$\delta / kT = (\ln \alpha_g - \ln \alpha_0) / (E_g - E_0),$$

$$\alpha_g = -65 + 1.88T + (8694 - 10.31T)x,$$

$$E_g(x, T) = -0.295 + 1.87x - 0.28x^2 + 10^{-4}(6 - 14x + 3x^2)T + 0.35x^4$$

The meaning of the parameter α_g is that $\alpha = \alpha_g$ when $E = E_g$, the absorption coefficient at the band gap energy. When $E < E_g$, $\alpha < \alpha_g$, the absorption coefficient obeys the Urbach rule in Eq. (14).

The spectral dependence of the absorption coefficient α well above E_g can be defined as follows

$$\alpha = \alpha_g \exp [\beta (E - E_g)]^{1/2} \quad (15)$$

where the parameter β depends on the alloy composition and temperature,

$$\beta(T, x) = -1 + 0.083T + (21 - 0.13T)x.$$

References

1. K. Jozwikowski and A. Rogalski, "Computer modeling of dual-band HgCdTe photovoltaic detectors," *J. Appl. Phys.*, vol. 90 (3), pp. 1286-1291, 2001.
2. M.B. Reine, A. Hairston, P.O'Dette, S.P.Tobin, F.T.J.Smith and B.L.Musicant, "Simultaneous MW/LW dual band MOVPE HgCdTe 64x64 FPAs," *Proceedings of SPIE*, vol. 3379, pp. 200-212, 1998.
3. ATLAS User's Manual, Device Simulation Software, SILVACO International, Santa Clara, CA 95054.
4. P.K. Saxena and P. Chakrabarti, "Computer modeling of MWIR single heterojunction photodetector based on mercury cadmium telluride," *Infrared Physics & Technology*, vol.52, pp.196-203, 2009.
5. P.K.Saxena, "Modeling and simulation of HgCdTe based p+n-n+ LWIR photodetector," *Infrared Physics & Technology*, vol. 54, pp. 25-33, 2011.
6. J. Chu, Z. Mi and D. Tang, "Band to band absorption in narrow-gap Hg_{1-x}Cd_xTe semiconductors," *J. Appl. Phys.*, vol. 71, pp. 3955-3961, 1992.

The Doping Effect Simulation on the OLED Devices Using ATLAS

Introduction

Organic light emitting diodes (OLEDs) have attracted great attention for full-color flat-panel displays since the demonstration of efficient electroluminescent devices [1]. Due to electrical doping of the electron and hole transport layer with an intrinsic emission layer sandwiched in between OLED, the devices have reached high performance and high luminance at low voltage.

In this article, we show the doping effect of the 2 layer NPB and Alq3 with C545T as the dopant using the 2 Dimensional Device Simulator ATLAS [2]. The electrical characteristics as the I-V curve and the local free carrier densities and ionized trapped charge densities were considered in this article using ATLAS. The Cole-Cole impedance [3] plot of the powerful method on characterizing many of the electrical properties of materials show the effective to doping effects.

Device Structure and Simulation Model

The simulated devices for the multilayer structure consist of ITO, NPB(65nm), Alq3(60nm), and LiF/Al for the without-doping device; and ITO, NPB(65nm), Alq3/C545T(30nm), Alq3(30nm) and LiF/Al for the with-doping device.

Figure 1 shows the simulated organic electronic device thickness and the energy diagram with LUMO and HOMO. The work function of ITO was chosen 5.05eV and LiF/Al was chosen the same energy with LUMO of the Alq3 as 3.0eV from the vacuum energy level. The hole trapped level of dopant, C545T, is 0.19eV from LUMO of Alq3 and the electron trapped level of dopant is 0.13eV from HOMO of Alq3.

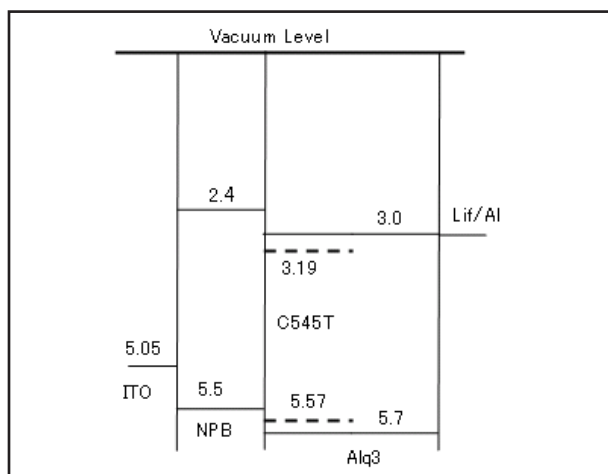


Figure 1. Schematic energy diagram and thickness of the simulated device.

Hopping Mobility for the Doping

The intrinsic of organic layer has the constant value as the zero-field mobility. But when the dopant was introduced to into organic layer, the mobility should be consider the double peak gaussian distribution along the energy as like the Figure 2.

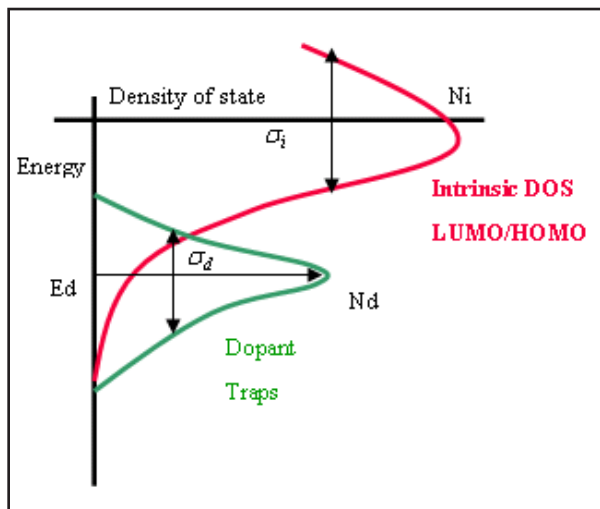


Figure 2. The effective transport hopping energy model and defines the defects using a double peak Gaussian distribution [4].

Figure 3. shows that the double peak Gaussian distribution should be considered mobility due to the doping level.

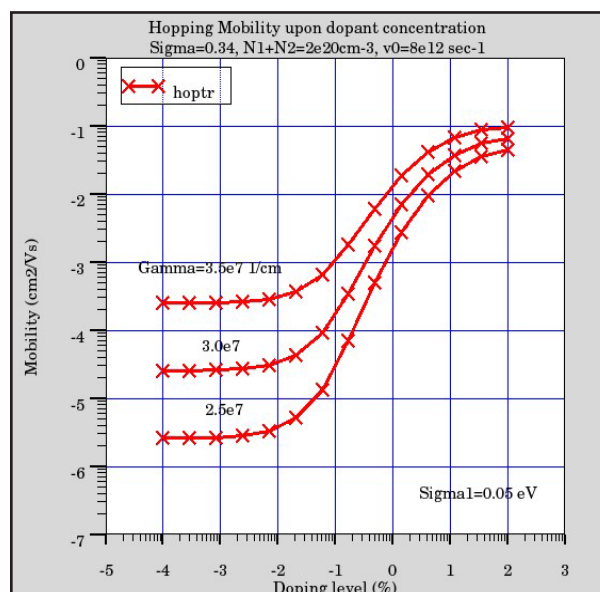


Figure 3. Charge carrier mobility in doped semiconducting polymers [5].

For example, when the doping level is below 1e-2 %, which is the intrinsic organic layer, the mobility is 2.5e-4 [cm²/Vs] at the Gamma=3.0e7 [6], but when the doping level is 10%, then the mobility increased to 4e-2 [cm²/Vs]. The doping is very effective for mobility in this case.

Dopant Effect on Transport Process

The recombination process for free carriers and charged dopant can be treated as the attractive Coulombic interaction between the free carrier and trapped charges plus the dopant's dipole because most dopant molecules are polar molecules.

The exciton generation rates on host and dopant for the singlet materials arising from the electron-hole recombination[6].

Simulation Results and Discussion

In the simulation of electrical process, the energy levels (HOMO and LUMO) are shown in Figure 1. The mobility depends on the doping level was considered as Figure 3. These are the key input data for the OLED electrical process simulation.

At first, we simulated the without dopant device using the structure as in Figure 1.

The free carrier concentration distribution at 9V on the anode is shown in Figure 4. At the 65nm of the interface NPB/Alq3 has the maximum carrier concentration.

For the device with dopants in the emitting layer, Alq3, as like Figure 5, there are electrons and holes trapped by dopants, and the trapped charge modifies the carrier transport process and their distribution in the device. With ATLAS, the organic device with dopant was simulated the free carrier concentration and trapped carrier concentration very clearly and simultaneously.

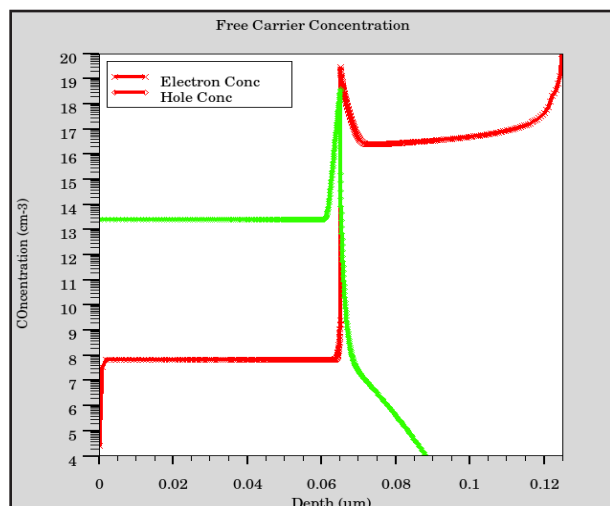


Figure 4. Free Carrier concentration profile without dopant device

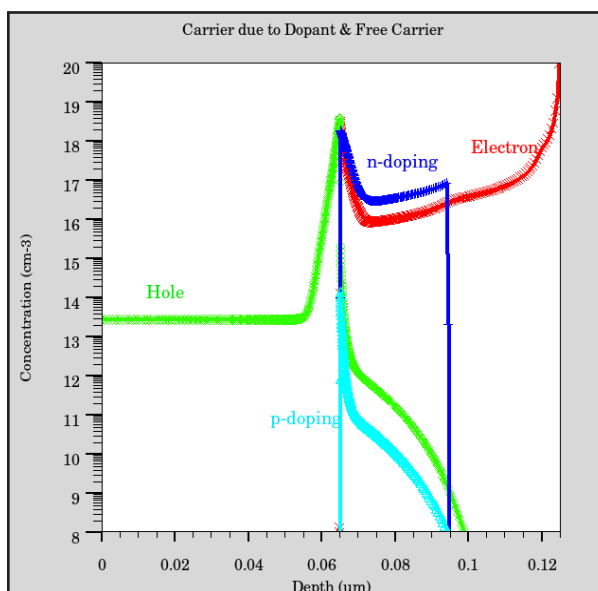


Figure 5. Free Carrier and trapped electron and hole concentration of 1.0% dopant device.

The comparison of the recombination rate at 9V with and without dopant is shown in Figure 6. The free carrier recombination rate for the device without dopant is confined to a very narrow region nearby the NPB/Alq3 interface. But for the device with dopant in the emitting layer, it could be observed that the free carrier recombination profile has been affected by the existing dopant and became broader. So the total recombination rate with dopant is greatly enhanced compared the without dopant device.

Finally the I-V characteristics for the multilayer devices with 4 different doping level are shown in Figure 7. The dopant effect can be simulated using ATLAS from getting the IV curve and it could be compared to measured data which is in good agreement.

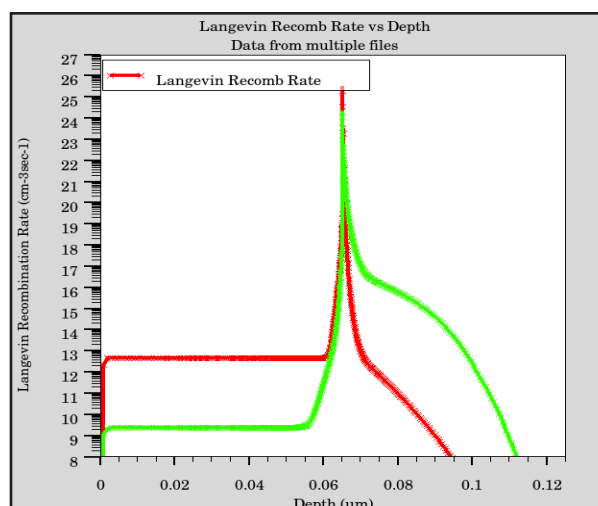


Figure 6. Langevin Recombination rate profiles

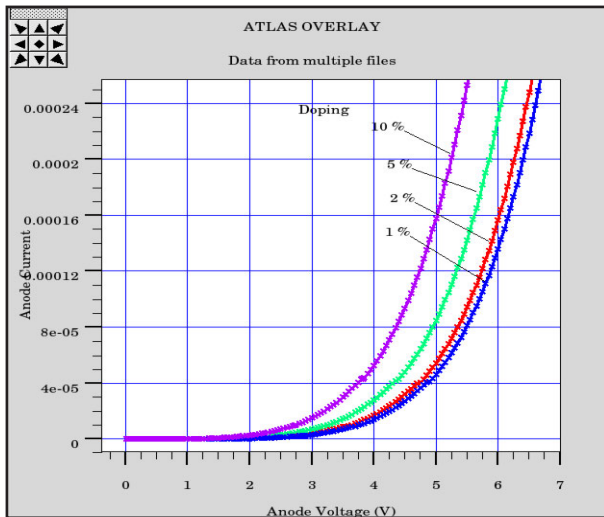


Figure 7. I-V characteristics with different doping ratios.

Impedance Spectroscopy Method

The measurement of the bias and frequency-dependent device capacitance is a well-established technique for the investigation of conductivity, doping and trap states in organic semiconductors. In ATLAS, with ac analysis, the Cole-Cole plot could get the Z parameters or Y parameters.

Typical data of the complex impedance $Z = \text{Re}[Z] - \text{Im}[Z]$ are shown in Figure 8 for the organic device with and without dopant.

Using this Impedance Spectroscopy, the Cole-Cole plot could be converted as shown in Figure 9 and 10.

Figure 9 shows this without the dopant and Figure 10 shows the 0.5% dopant effect.

Conclusion

We have presented efficiency calculation of the electrical characteristics for the OLED with dopant in the host material based due to the dopant level.

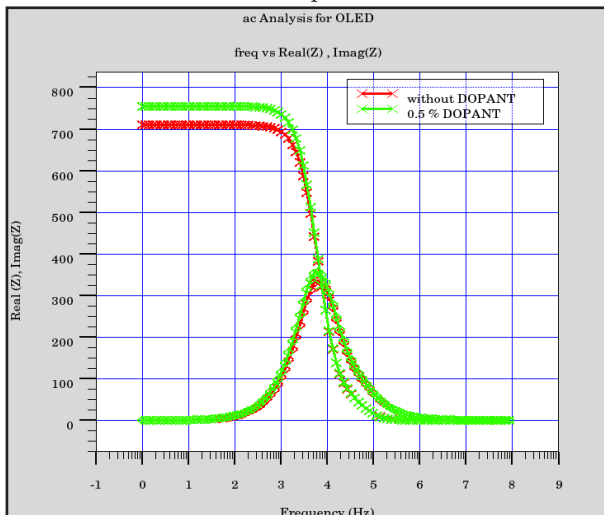


Figure 8. Impedance Spectroscopy method of Z Parameter.

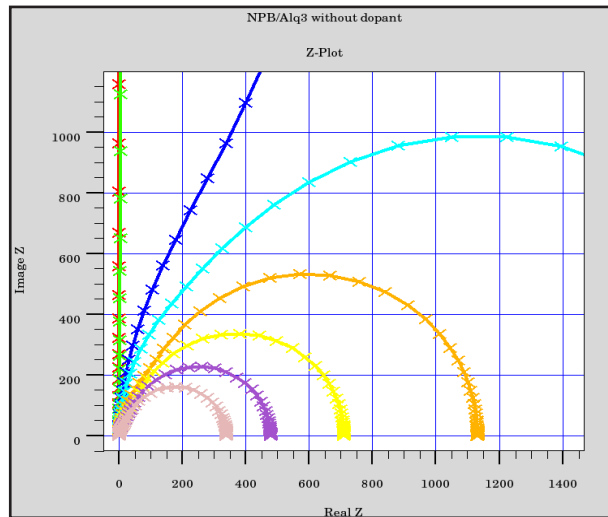


Figure 9. Cole-Cole plot without dopant.

We have also shown the Cole-Cole plot with the Impedance Spectroscopy method for the investigation of the conductance using ATLAS Device simulator.

Reference

- [1] C. W. Tang, S. A. Vanslyke, Appl. Phys. Lett. 51 (1987) 913.
- [2] ATLAS User's Manual, Baseline 2010 Version
- [3] H. Naito, "Impedance Spectroscopy of the Organic Electronic Devices", JSAP. 76 No. 11, pp.1252-1258 (2007) Japanese
- [4] Arkhipov, V.I., P. Heremans, E.V. Emelianova, G.J. Adriaenssens, H. Bassler, "Charge carrier mobility in doping disordered organic semiconductors", Journal of Non-Crystalline Solids, Vol. 338-340 (2004): 603-606.
- [5] V.I. Arkhipov, P. Heremans, E.V. Emelianova, G.J. Adriaenssens, H. Bassler, Applied Physics Letters, Vol. 82, No. 19, pp 3245-3247, 2003
- [6] ATLAS User's Manual, Chapter 15, Baseline 2010 Version

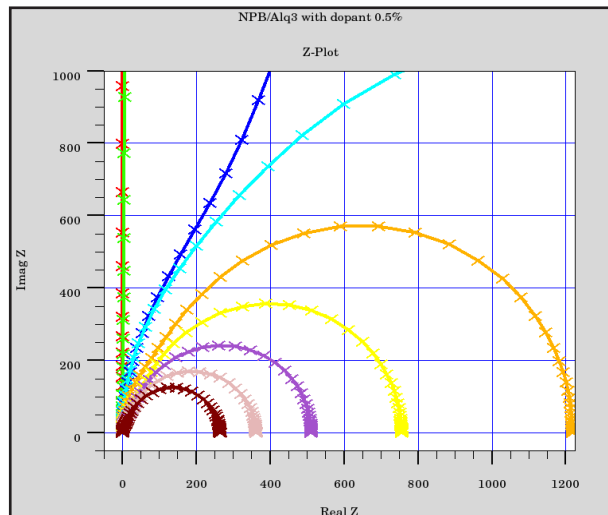


Figure 10. Cole-Cole plot with 0.5% dopant.

Using VICTORY Process to Simulate Thermal Oxidation of Silicon at High Pressures of Ambient Gases

Introduction

Developing ULSI silicon technology requires good control of dopant diffusion and minimizing defect formation during thermal oxidation. The use of high pressures of ambient gases can have a significant impact on ability to meet such requirements [1]. In particular, high pressure steam (~10atm) allows the growth of oxide films of the order of 1 μm in less than 2.5 hours at temperature as low as 800 C. At such low temperatures dopant redistribution is substantially reduced.

This paper demonstrates the ability of VICTORY Process to accurately model the thermal oxidation of silicon at high pressures. The 3D process simulation software VICTORY Process uses the same physical model as one implemented in ATHENA (2D process simulator). The model is briefly outlined below. Numerical results are compared with the experimental ones [1] and the good agreement is demonstrated. If plane silicon is thermally oxidized, both Silvaco's process simulators (VICTORY Process and ATHENA) give very close results. The paper shows that these results are also close to the results obtained by integration of the 1D kinetical equation obtained by DealGrove and Massoud [2,3]. These comparisons prove that the model is properly implemented in VICTORY Process and can be used to oxidize 3D structures at high pressures.

Physical Model

The main physical parameters that determine the kinetics of silicon oxidation are

- linear rate, B/A
- parabolic rate B
- Massoud rate R

These rates are normally measured and specified at pressure equal to 1 atm. To describe the pressure dependence of these parameters VICTORY Process and ATHENA use the relations suggested by R. Razouk, L. Lie and E. Deal [1]. According to their model, all three rates are multiplied by correspondent pressure factors such that the resulting rates become:

$$\frac{B}{A} = \left(\frac{B}{A}\right)_1 \cdot P^{l.pdep}$$

$$B = B_1 \cdot P^{p.dep}$$

$$R = R_1 \cdot P^{thin.p}$$

where index 1 denotes the terms taken at pressure equal to one atm., $l.pdep \approx p.dep \approx thin.p \approx 1$ being calibrating parameters. The resulting rates are used to calculate the microscopical parameters like diffusion and reaction coefficients which are used in 3D mathematical model [4].

Numerical and Experimental Results

Using the experimental results from [1] we obtained the following values for the linear and parabolic rates at $T=900\text{ C}$ (dry) and $P=1\text{atm}$: $(B/A)_1 = 0.00462\ \mu\text{m}/\text{min}$ and $B_1 = 0.00247\ \mu\text{m}^2/\text{min}$. The rates are assumed to obey the Arrhenius relations:

$$\left(\frac{B}{A}\right)_1 = \text{lin.h.0} \cdot \exp\left(\frac{-\text{lin.l.e}}{kT}\right)$$

$$B_1 = \text{par.h.0} \cdot \exp\left(\frac{-\text{par.h.e}}{kT}\right)$$

with the user specified parameters lin.h.0 , lin.l.e , par.h.0 , par.l.e . The powers describing the pressure dependence are taken as following: $l.pdep = 0.8$, $p.dep=1$, $thin.p=1$. All other oxidation parameters (e.g. Massoud rate, silicon-oxide expansion coefficient etc.) are equal to its default values specified in Silvaco's material database (smdb). The described values are supplied using the deck command:

```
MATERIAL material=silicon dry02 \
lin.h.0 = 0.00462 lin.h.e = 0.0 l.pded = 0.8 \
par.h.0 = 0.00247 par.h.e = 0.0 p.pdep = 1 \
thin.p = 1
```

Different times and pressures are set by using commands like :

```
DIFFUSE time=30 temperat=900 dry02 pressure=10
```

To compare our results with the experimental ones, we simulated oxidation of plane silicon at the conditions chosen in the experiment. Namely, at four different pressures (1, 5, 10, 20) atm., times being equal to (0.5, 1, 2, 3) hours. Experimental and numerical results are compared on the Figure 1.

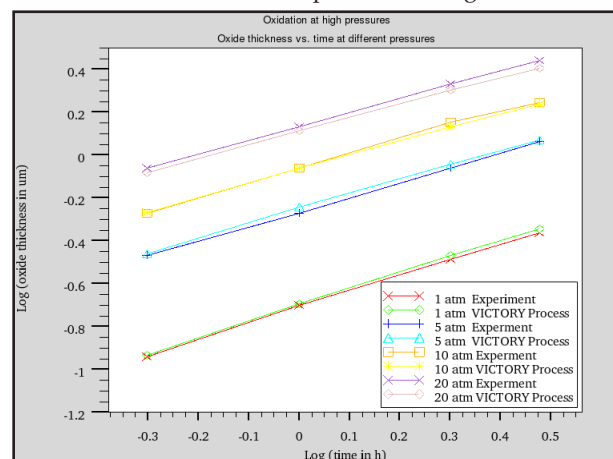


Figure 1. Oxide thickness vs. oxidation time for silicon oxidized in dry oxygen at temperature of 900 C and at pressures of 1, 5, 10 and 20 atm.

VICTORY Process, ATHENA and Analytical Results

The 3D implementation of the highpressure oxidation model in VICTORY Process can be partly verified by comparing its results with the results obtained by ATHENA (2D) and with the results obtained by integration of the 1D Deal-Grove-Massoud equation:

$$\frac{dx}{dt} = \frac{B}{A + 2x} + R$$

with the initial condition $x(t=0) = x_0$ and x_0 being initial oxide thickness (20Å in our case). The 1D model uses the same values of oxidation rates. The results are plotted on

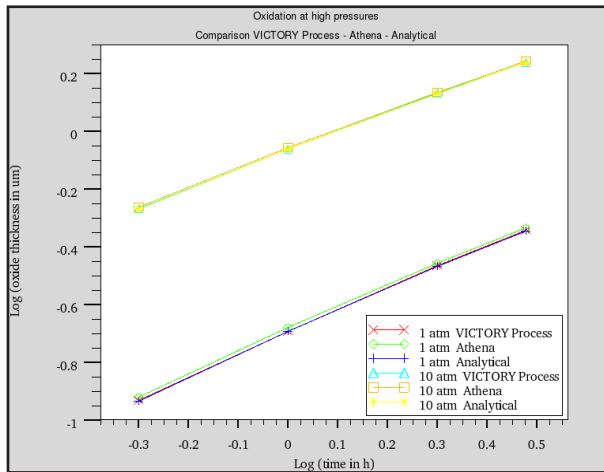


Figure 2. Oxide thickness vs. oxidation time for silicon oxidized in dry oxygen at temperature of 900 C at pressure of 1 and 10 atm. Comparison of the numerical results obtained using VICTORY Process, ATHENA and 1D integration of DealGroveMas-soud equation.

the Figure 2. The figure demonstrates that for the oxidation of plane silicon the results are very close.

Conclusion

In this paper we demonstrated the ability of VICTORY Process to simulate thermal oxidation of silicon at high pressures in 3D.

References

- [1] Reda R. Razouk, Liang N. Lie and Bruce E. Deal. Kinetics of High Pressure Oxidation of Silicon in Pyrogenic Steam J. Electrochem. Soc. : SolidState Science and Technology, vol. 128, no 10, pp.22142220, Oct 1981.
- [2] B.E.Deal and A.S.Grove General Relationship for the Thermal Oxidation of Silicon Journal of Applied physics, vol. 36, no 12, Dec 1965.

Hints, Tips and Solutions

Q. Can I export the 3D structures created by VICTORY Cell or VICTORY Process to a format compatible with ANSOFT ANSYS?

A. Yes. SILVACO provides the tool ANSYSExporter which establishes the link between SILVACO software and ANSOFT ANSYS. ANSYSExporter is fully integrated within the SILVACO environment and can be called by means of a deck statement from DeckBuild or used as a stand-alone tool via command line.

This link between SILVACO format and ANSOFT ANSYS is realized via the stereolithography file format (STL) which is a standard format for describing the surface geometry of 3D structures. It is compatible with the tool ICEM CFD Tetra/Prism (ANSYS framework) from ANSOFT and with many other third party CAD tools. Files, containing data in STL format, have an extension '.stl'.

The STL format represents structures as a set of closed tessellated surfaces. Each surface outlines parts of the structure consisting of the same material or belonging to the same SDB region. It means that a single 3D structure, composed of several materials or regions, can be represented as a set of STL files (one for each region or material).

The ANSOFT ANSYS tool ICEM CFD Tetra/Prism can load multiple STL files to compose a single 3D structure and can build the unstructured tetrahedral mesh for the full structure, while maintaining a consistent mesh between the parts. This mesh can then be exported into various formats which are suitable for various tools in the ANSYS framework. For more details please consult the ANSYS user manual from ANSOFT.

ANSYSExporter can be used with structures represented by a volume (tetrahedral) mesh and to structures represented by a surface (triangle) mesh enclosing the regions.

Q. How can I export VICTORY Cell structures to a format compatible with ANSYS?

A. You can interface with the ANSYS framework from ANSOFT either via simulation deck or by exporting any structure created by VICTORY Cell using ANSYSExporter. The result of the export is a set of .stl files, which you need to start the simulation in the ANSYS framework. When the ANSYSExporter is applied to structures represented by a prismatic mesh, they are automatically internally converted to tetrahedral meshes before export.

1. Interface via simulation deck.

After saving the structure with the VICTORY Cell deck statement

```
STRUCT outfile=myVcellStructure.str
```

add the following deck statement

```
ANSYSEXPORTER stl myVcellStructure.str  
myVcellStructure
```

When this deck statement is executed several .stl files with the names

```
myVcellStructure_<material_name>.stl
```

are created.

2. Interface via saved VICTORY Cell structure.

You can convert the structures, created by VICTORY Cell, to the set of .stl files by calling the ANSYSExporter from the system command line. If your file has the name myVcellStructure.str just call

```
ANSYSEXPORTER stl myVcellStructure.str  
myVcellStructure
```

on the system command line.

Note: The file name (including extension) is case sensitive.

Once you have executed this command, several .stl files with the names

```
myVcellStructure_<material_name>.stl
```

are created.

You can process the resulting .stl files with the ANSOFT tool ICEM CFD Tetra/Prism. For more details please consult the ANSYS user manual from ANSOFT.

Q. How can I export VICTORY Process structures to a format compatible with ANSYS?

A. You can interface with the ANSYS framework from ANSOFT either via the simulation deck or by exporting any structure created by VICTORY Process using the ANSYSExporter. The result of the export is the set of the .stl files, which you need to start the simulation in the ANSYS framework.

1. Interface via simulation deck.

First, you need to export the VICTORY Process structure into an appropriate format for the ANSYSExporter with the following deck statement:

```
EXPORT surfaces name=myVprocessStructure_
surf
```

then add the statement for converting the results to the set of .stl files:

```
ANSYSEXPORTEr stl myVprocessStructure_surf.
str myVprocessStructure
```

Note : You should use a VICTORY Process version greater or equal 2.17.3.C.

After this statement has been executed several .stl files with the names

```
myVprocessStructure_<material_name>.stl
```

are created.

2. Interface via structure saved with STRUCT command

If the structure file was created by VICTORY Process by means of the deck statement

```
STRUCT outfile=myVprocessStructure.str
```

you need a deck with the following statements to create the .stl files suitable for the ANSYS framework.

```
go victoryprocess
INIT infile=myVprocessStructure.str
EXPORT surfaces name=myVprocessStructure_surf
ANSYSEXPORTEr stl myVprocessStructure_surf.
str myVprocessStructure
```

By executing this deck within DeckBuild several .stl files with the names

```
myVprocessStructure_<material_name>.stl
```

are created.

3. Interface via structure created with EXPORT command

If the structure file was created by VICTORY Process by means of one of the following statements:

```
EXPORT surfaces name=myVprocessStructure.str
[parameters]
EXPORT process name=myVprocessStructure.str
[parameters]
EXPORT device name=myVprocessStructure.str
[parameters]
```

you can convert this structure to several .stl files by calling ANSYSExporter from the system command line. It is recommended to use the 'surfaces' mode of the EXPORT command when creating the structures for processing with the ANSYSExporter.

If your file is named myVcellStructure.str just type

```
ANSYSEXPORTEr myVcellStructure.str
myVcellStructure
```

on the system command line. Note that the file name (including extension) is case sensitive.

Once you have executed this command, several .stl files with the names

```
myVcellStructure_<material_name>.stl
```

are created.

You can process the resulting .stl files with the ANSOFT tool ICM CFD Tetra/Prism. For more details please consult the ANSYS user manual from ANSOFT.

Call for Questions

If you have hints, tips, solutions or questions to contribute, please contact our Applications and Support Department
Phone: (408) 567-1000 Fax: (408) 496-6080
e-mail: support@silvaco.com

Hints, Tips and Solutions Archive

Check out our Web Page to see more details of this example plus an archive of previous Hints, Tips, and Solutions
www.silvaco.com



JOIN THE WINNING TCAD TEAM

USA Headquarters:

Silvaco, Inc.

4701 Patrick Henry Drive, Bldg. 2
Santa Clara, CA 95054 USA

Phone: 408-567-1000

Fax: 408-496-6080

sales@silvaco.com

www.silvaco.com

Worldwide Offices:

Silvaco Japan

jpsales@silvaco.com

Silvaco Korea

krsales@silvaco.com

Silvaco Taiwan

twsales@silvaco.com

Silvaco Singapore

sgsales@silvaco.com

Silvaco Europe

eusales@silvaco.com

SILVACO